GEOPHYSICS, VOL. 69, NO. 3 (MAY-JUNE 2004); P. 825–839, 13 FIGS., 2 TABLES.
10.1190/1.1759469

The physics and simulation of wave propagation at the ocean bottom

José M. Carcione* and Hans B. Helle‡

ABSTRACT

We investigate some aspects of the physics of wave propagation at the ocean bottom (ranging from soft sediments to crustal rocks). Most of the phenomena are associated to the presence of attenuation. The analysis requires the use of an anelastic stress-strain relation and a highly accurate modeling algorithm. Special attention is given to modeling the boundary conditions at the ocean-bottom interface and the related physical phenomena. For this purpose, we further develop and test the pseudospectral modeling algorithm for wave propagation at fluid-anelastic solid interfaces. The method is based on a domain-decomposition technique (one grid for the fluid part and another grid for the solid part) and the Fourier and Chebyshev differential operators. We consider the reflection, transmission, and propagation of seismic waves at the ocean bottom, modeled as a plane boundary separating an acoustic medium (ocean) and a viscoelastic solid (sediment). The main physical phenomena associated with this interface are illustrated, namely, amplitude variations with offset, the Rayleigh window, and the propagation of Scholte and leaky Rayleigh waves. Modeling anelasticity is essential to describe these effects, in particular, amplitude variations near and beyond the critical angle, the Rayleigh window, and the dissipation of the fundamental interface mode. The physics of wave propagation is investigated by means of a plane-wave analysis and the novel modeling algorithm. A wavenumber–frequency domain method is used to compute the reflection coefficient and phase angle from the synthetic seismograms. This method serves to verify the algorithm, which is shown to model with high accuracy the Rayleigh-window phenomenon and the propagation of interface waves. The modeling is further verified by comparisons with the analytical solution for a fluid-solid interface in lossless media, with source and receivers away from and at the ocean bottom. Using the pseudospectral modeling code, which allows general material variability, a complete and accurate characterization of the seismic response of the ocean bottom can be obtained. An example illustrates the effects of attenuation on the propagation of dispersive Scholte waves at the bottom of the North Sea.

INTRODUCTION

The problem of reflection, refraction, and propagation at a plane boundary separating an acoustic medium (fluid) and a viscoelastic solid has practical application in seismic exploration, seismology, foundation engineering, and nondestructive testing of materials (e.g., Roever et al., 1959; Ash and Paige, 1985; Stephen, 1986; Brekhovskikh and Lysanov, 1991; Robertsson and Levander, 1995; Lomnitz et al., 2002). In seismic exploration, the relevant fluid-solid interface is the ocean bottom, whose properties are useful for data processing of multicomponent seismic surveys acquired at the sea floor. Knowledge of S-wave velocities is required for static corrections and imaging of mode-converted PS-waves (Muyzert, 2000). Shear velocity is also important for multiple removal. The viscoelastic constitutive equation models the different attenuation mechanisms present in ocean-bottom sediments (e.g., Hamilton, 1972).

In lossless media, Ergin (1952) investigated the reflection-transmission problem for different sets of the acoustic parameters, and also considered incident P- and S-waves from the solid. The seismic reflection-transmission problem in lossless media has also been studied by Berteussen and Alstad (1985), who considered various cases (i.e., different values of the P-wave velocity, S-wave velocity, and density of the ocean-bottom sediment).

There exist two interface waves at a fluid-solid interface: one that travels mainly in the liquid, and the other that has most of its energy in the solid. Cagniard (1962) investigated the first type of waves, calling them Scholte waves. In general, the second type is a leaky Rayleigh wave, propagating along the interface with attenuation (Strick, 1959; Auld, 1985). The leaky

Manuscript received by the Editor November 17, 2002; revised manuscript received July 7, 2003.
*Istituto Nazionale di Oceanografia e di Geofisica Sperimentale (OGS), Borgo Grotta Gigante 42c, 34010 Sgonico, Trieste, Italy. Fax: 0039 040 327521. E-mail: jcarcione@ogs.trieste.it.
‡Norsk Hydro a.s., O & E Research Centre, N-5020 Bergen, Norway. Fax 47 55 996970. E-mail: hans.b.helle@hydro.com.

Rayleigh wave at a lossless fluid-solid interface decays with depth in the bottom but corresponds to a propagating body wave in the fluid (with characteristics similar to head waves). The amplitude of this wave increases in the fluid away from the interface (Farnell, 1970; Auld, 1985) (Rayleigh discarded these solutions on the basis of this behaviour). Leaky Rayleigh waves can explain arrivals of supersonic waves observed in the Canadian Artic (Chamuel, 1991). See Padilla et al. (1999), for experimental evidence of the existence of these two types of waves. The anelastic Scholte wave has been investigated by Favretto-Anrès (1996), Favretto-Anrès and Rabau (1997) and Favretto-Anrès and Sessarego (1999). These waves are important in studying the acoustic properties of sediments in coastal waters (Rauch, 1980). Moreover, they can be used to estimate shear-wave parameters, such as shear-wave velocity and quality factor (e.g., Nolet and Dorman, 1996).

In the first part of the paper, we study the physics of anelastic wave propagation for material properties that are not commonly encountered. Under such circumstances, a number of interesting phenomena arise, which are discussed in the paper. Borcherdt et al. (1986) present theoretical and experimental results for a water-stainless steel interface, where the phenomenon called the Rayleigh window occurs (e.g., Carcione, 2001, p. 214). This viscoelastic effect implies that the energy incident on the boundary at angles within that window is substantially transmitted. The theory has also been applied to ocean-bottom reflections. To our knowledge, the Rayleigh window has not been simulated with direct grid methods [see Carcione et al. (2002) for a brief description of these methods].

Stephen (1986) has used the finite-difference method to study seismo-acoustic problems. He shows simulations where all the wave types are illustrated. His modeling method is heterogeneous, where the boundary condition at the fluid-solid interface is implicitly modeled. Recently, Komatitsch et al. (2000) developed a spectral finite-element approach to explicitly model the boundary condition. Similarly, van Vossen et al. (2002) present an explicit method and show that only five grid points per wavelength are needed for accurate calculations with the finite-difference method. Interface waves are exponentially damped away from the interface, so they require denser grid points than body waves. Therefore, an accurate simulation of interface waves requires, in general, a special boundary treatment, particularly when using finite-difference (e.g., Mittet, 2002) and pseudospectral methods. All the methods mentioned above consider a lossless solid and, therefore, phenomena like the Rayleigh window and attenuation of interface waves cannot be modeled. Moreover, previous studies based on anelastic constitutive equations, have not considered these phenomena. Anelastic wave modeling has been used, for instance, to investigate the difference between intrinsic dissipation and attenuation due to scattering at the sea floor (Stephen and Swift, 1994).

We study the physics of wave propagation by using a domain-decomposition method based on pseudospectral differential operators. Explicit modeling of the slip boundary condition is done by using domain decomposition techniques and pseudospectral methods. The Fourier method is used along the interface direction and the Chebyshev method is used along the direction perpendicular to the interface. The approach for viscoelastic waves is illustrated in Carcione (1991, 1994a). Modeling examples are given in Kessler and Kosloff (1991) and Tessmer et al. (1992) for elastic media, and Carcione (1996) for viscoelastic media. Here, we consider a flat interface, but the algorithm can be extended to model topographic features of the ocean bottom by using a mapping transformation (e.g., Carcione, 1994b).

The physics is mainly illustrated for a homogeneous ocean bottom. In inhomogeneous media, interface waves are dispersive and several modes can propagate. Their phase and group velocities versus frequency can be computed by using the method of Runge-Kutta for a continuous velocity profile and the Thomson-Haskell method for a stack of homogeneous layers (Takeuchi and Saito, 1972). McMechan and Yedlin (1981) illustrate the use of these dispersion curves for the interpretation of interface waves in marine seismic surveys (Bohlen et al., 1999; Glangeaud et al., 1999). An example of propagation in the presence of an inhomogeneous ocean bottom illustrates the propagation of dispersive interface modes.

The paper is organized as follows. The first five sections provide the theory. Then, the domain-decomposition method for anelastic fields is described. The following sections introduce the geo-acoustic properties and deal with the reflection coefficients, including the Rayleigh-window phenomenon and the amplitude-variation-with-offset (AVO) analysis (a test of the algorithm is performed). Next, we present the results for the interface waves, including a test of the modeling algorithm and the analysis of the physics by solving the dispersion equation. Finally, we present a simulation of a real seismogram.

EQUATIONS OF MOTION

The time-domain equations for propagation in a heterogeneous viscoelastic medium can be found in Carcione (2001, p. 110). The anelasticity is described by the standard linear solid, also called the Zener model, that gives relaxation and creep functions in agreement with experimental results (Zener, 1948).

The two-dimensional velocity-stress equations for anelastic propagation in the (x, z)-plane, assigning one relaxation mechanism to dilatational anelastic deformations ($\nu = 1$) and one relaxation mechanism to shear anelastic deformations ($\nu = 2$), can be expressed by:

1) Euler-Newton's equations:

$$\dot{v}_x = \frac{1}{\rho}(\sigma_{xx,x} + \sigma_{xz,z}) + f_x, \tag{1}$$

$$\dot{v}_z = \frac{1}{\rho}(\sigma_{xz,x} + \sigma_{zz,z}) + f_z, \tag{2}$$

where v_x and v_z are the particle velocities, σ_{xx}, σ_{zz} and σ_{xz} are the stress components, ρ is the density, and f_x and f_z are the body forces. A dot above a variable denotes time differentiation, and the subindices, "x" and "z" indicate spatial derivatives with respect to the Cartesian coordinates.

2) Constitutive equations:

$$\dot{\sigma}_{xx} = k(v_{x,x} + v_{z,z} + e_1) + \mu(v_{x,x} - v_{z,z} + e_2), \tag{3}$$

$$\dot{\sigma}_{zz} = k(v_{x,x} + v_{z,z} + e_1) - \mu(v_{x,x} - v_{z,z} + e_2), \tag{4}$$

$$\dot{\sigma}_{xz} = \mu(v_{x,z} + v_{z,x} + e_3), \tag{5}$$

where e_1, e_2, and e_3 are memory variables, and k and μ are the unrelaxed (high-frequency) bulk and shear moduli, respectively.

3) Memory variable equations:

$$\dot{e}_1 = \left(\frac{1}{\tau_\epsilon^{(1)}} - \frac{1}{\tau_\sigma^{(1)}}\right)(v_{x,x} + v_{z,z}) - \frac{e_1}{\tau_\sigma^{(1)}}, \quad (6)$$

$$\dot{e}_2 = \left(\frac{1}{\tau_\epsilon^{(2)}} - \frac{1}{\tau_\sigma^{(2)}}\right)(v_{x,x} - v_{z,z}) - \frac{e_2}{\tau_\sigma^{(2)}}, \quad (7)$$

$$\dot{e}_3 = \left(\frac{1}{\tau_\epsilon^{(2)}} - \frac{1}{\tau_\sigma^{(2)}}\right)(v_{x,z} + v_{z,x}) - \frac{e_3}{\tau_\sigma^{(2)}}, \quad (8)$$

where $\tau_\sigma^{(\nu)}$ and $\tau_\epsilon^{(\nu)}$ are material relaxation times, corresponding to dilatational ($\nu = 1$) and shear ($\nu = 2$) deformations. We recall that in a 2-D world, $\mu = \rho V_S^2$ and $k = \rho(V_P^2 - V_S^2)$, where V_P an V_S are the compressional- and shear-wave unrelaxed velocities.

The equations for the viscoacoustic medium are obtained from equations (1)–(8) by setting $\sigma_{xx} = \sigma_{zz} \equiv \sigma$, $\sigma_{xz} = 0$ and $\mu = 0$. Then, the equations of motion read

$$\dot{v}_x = \frac{\sigma_{,x}}{\rho} + f_x, \quad (9)$$

$$\dot{v}_z = \frac{\sigma_{,z}}{\rho} + f_z, \quad (10)$$

where

$$\dot{\sigma} = k(v_{x,x} + v_{z,z} + e_1), \quad (11)$$

together with the memory-variable equation (6). The extension of the theory to many dissipation mechanisms is straightforward (Carcione, 2001, p. 210).

Complex velocities

The P- and S-wave complex velocities, $\bar{v}_P$ and $\bar{v}_S$, are the key quantities to obtain the phase velocities and attenuation factors. They are defined by

$$\rho\bar{v}_P^2(\omega) = kM_1(\omega) + \mu M_2(\omega), \quad \text{and} \quad \rho\bar{v}_S^2(\omega) = \mu M_2(\omega) \quad (12)$$

(Christensen, 1982; Carcione, 2001, p. 65, 85), where ω is the angular frequency, and

$$M_\nu = \frac{\tau_\sigma^{(\nu)}}{\tau_\epsilon^{(\nu)}}\left(\frac{1 + i\omega\tau_\epsilon^{(\nu)}}{1 + i\omega\tau_\sigma^{(\nu)}}\right), \quad \nu = 1, 2 \quad (13)$$

are the Zener complex moduli, and $i = \sqrt{-1}$.

The relaxation times can be expressed as

$$\tau_\epsilon^{(\nu)} = \frac{\tau_0}{Q_0^{(\nu)}}\left[\sqrt{{Q_0^{(\nu)}}^2 + 1} + 1\right], \quad \tau_\sigma^{(\nu)} = \tau_\epsilon^{(\nu)} - \frac{2\tau_0}{Q_0^{(\nu)}}, \quad (14)$$

where τ_0 is a relaxation time such that $1/\tau_0$ is the center frequency of the relaxation peak and $Q_0^{(\nu)}$ are the minimum quality factors. For the angular frequency ω, we take $\tau_0\omega = 1$. This means that we place the center of the relaxation peak at the working frequency.

The quality factor, $Q_0^{(1)}$, associated with the bulk modulus, is obtained from the relation

$$\frac{1+\sigma}{Q_0^{(1)}} = \frac{3(1-\sigma)}{Q_P} - \frac{2(1-2\sigma)}{Q_0^{(2)}},$$

$$\sigma = [(V_P/V_S)^2 - 2]/2[(V_P/V_S)^2 - 1] \quad (15)$$

(Winkler and Nur, 1979), where σ is Poisson's ratio, Q_P is the P-wave quality factor, and $Q_S = Q_0^{(2)}$ is the S-wave quality factor.

Similarly, the complex velocity for the viscoacoustic medium is obtained from

$$\rho\bar{v}_P^2(\omega) = kM_1(\omega). \quad (16)$$

PROPAGATION CHARACTERISTICS

A general plane-wave solution for the particle velocity field $\mathbf{v} = (v_x, v_z)$ is

$$\mathbf{v} = i\omega\mathbf{U}\exp[i\omega(t - s_x x - s_z z)], \quad (17)$$

where s_x and s_z are the components of the complex slowness vector, t is the time variable, and $\mathbf{U}$ is a complex vector. For homogeneous viscoelastic waves, the directions of propagation and attenuation coincide, and

$$s_x = \sin\theta/\bar{v}, \quad s_z = \cos\theta/\bar{v}, \quad (18)$$

where θ is the propagation angle, measured with respect to the z-axis, and $\bar{v} = 1/s$, ($s^2 = s_x^2 + s_z^2$) is the complex velocity.

For homogeneous waves in isotropic media, the phase velocity and attenuation factors are given by

$$v_p = \left[\mathrm{Re}\left(\frac{1}{\bar{v}}\right)\right]^{-1} \quad \text{and} \quad \alpha = -\omega\mathrm{Im}\left(\frac{1}{\bar{v}}\right), \quad (19)$$

and the quality factor is

$$Q = \frac{\mathrm{Re}(\bar{v}^2)}{\mathrm{Im}(\bar{v}^2)} \quad (20)$$

(e.g., Carcione, 2001, p. 99, 105), where v is given in the previous section [equations (12)–(16)]. For interfaces waves, the complex velocity is given in the next sections.

THE SCHOLTE-WAVE DISPERSION EQUATION

The dispersion equation is obtained by requiring continuity of the normal components of the displacement and stress at the interface. Details can be found in Scholte (1942), Gusev et al. (1996), Meegan et al. (1999), Padilla et al. (1999), and Glorieux et al. (2002). Let us define

$$q = \frac{\bar{v}^2}{\bar{v}_{S_2}^2}, \quad a = \frac{\bar{v}_{S_2}^2}{\bar{v}_{P_2}^2}, \quad b = \frac{\bar{v}_{S_2}^2}{\bar{v}_{P_1}^2}, \quad (21)$$

where $\bar{v}$ is the complex velocity of the interface wave, and 1 denotes the fluid and 2 the solid. The dispersion equation of the Scholte wave can be expressed as

$$S(q) = 4\sqrt{1-q}\sqrt{1-aq} - (2-q)^2 - \left(\frac{\rho_1}{\rho_2}\right)q^2\sqrt{\frac{1-aq}{1-bq}} = 0 \quad (22)$$

(Brekhovskikh and Lysanov, 1991, p. 67). If $\rho_1 = 0$, this equation reduces to the dispersion equation for viscoelastic Rayleigh waves (e.g., Carcione, 2001, p. 104). Ansell (1972) obtained the roots of the dispersion equation by a detailed analysis in the complex wavenumber plane (see Padilla et al., 1999). The Riemann surface of function S has eight sheets, which correspond to different choices of the signs of the complex square roots $\sqrt{1-q}$, $\sqrt{1-aq}$, and $\sqrt{1-bq}$. In the lossless case, roots of the Scholte wave are real, whereas roots of the leaky Rayleigh wave are complex. Thus, the first wave travels without attenuation and the second decays along the interface. These surface waves are superpositions of inhomogeneous elastic waves, that is, the attenuation vector makes an angle of 90° with respect to the propagation vector. For Scholte waves, the attenuation vector is perpendicular to the interface, whereas for leaky Rayleigh waves, the attenuation vector has a nonzero projection on the interface.

In general, there are five causes of amplitude reduction: geometrical spreading, evanescent decay (diffraction), leaking, intrinsic energy loss, and scattering. The term decay can be used for all the cases, but the term attenuation applies to the last two causes. In the lossless 2D case, the Scholte wave travels without attenuation because it is not a leaking mode, but in 3D space it would decay because of geometrical spreading. On the other hand, the leaky Rayleigh wave decays for lossless media in both 3D and 2D media because in both cases it leaks.

The existence of the leaky wave is subject to the condition that the sound velocity in the liquid must be less than the shear velocity in the solid (this a necessary but not a sufficient condition). The leaky Rayleigh wave approaches the Rayleigh wave as the density of the liquid tends to zero. Hence, the Rayleigh wave in a vacuum solid interface is not the Scholte wave when the density of the liquid goes to zero. This applies to the rigid bottom case (shear velocity higher than water velocity). On the other hand, for the soft bottom case (shear velocity less than water velocity), the Scholte wave pole converges to the Rayleigh pole as the density of the water goes to zero (Rauch, 1980). Whereas the free Rayleigh wave always exists, the leaky Rayleigh wave does not (Brower et al., 1979). Most quasi-surface waves, corresponding to roots lying on lower Riemann sheets, are not always physically separable on experimental or numerical simulations due to their close association with body-wave phases. For instance, Phinney (1961) predicts a pseudo-P pulse coupled to the P-wave.

For a stiff fluid-solid interface, the leaky Rayleigh wave has a velocity slightly lower than the body-wave shear velocity, and the Scholte wave velocity is lower than the liquid sound velocity. As the solid becomes stiffer, the Scholte wave velocity approaches that of the liquid. As mentioned above, for soft solids (body-wave shear velocity lower than the sound velocity of the liquid), the Rayleigh-type root is not a physical solution. The leaky Rayleigh wave is also relevant in wave propagation in boreholes (Paillet and White, 1982).

Surface waves at liquid-porous media classify into three kinds. A true surface wave that travels slower than all the wave velocities (the generalization of the Scholte wave), a pseudo-Scholte wave that travels with a velocity between the shear-wave velocity and the slow-wave velocity (leaking energy to the slow-wave), and a pseudo-Rayleigh wave, which becomes the classical Rayleigh wave if the liquid density goes to zero (Holland, 1991; Edelman and Wilmanski, 2002).

MODELING AND DOMAIN-DECOMPOSITION METHOD

Two grids model the fluid and solid subdomains (labeled 1 and 2, respectively). The solution on each grid is obtained by using the Runge-Kutta method as time stepping algorithm and the Fourier and Chebyshev differential operators to compute the spatial derivatives in the horizontal and vertical directions, respectively (Carcione, 1992a, 1994a, 2001). In order to combine the two grids, the wave field is decomposed into incoming and outgoing wave modes at the interface between the solid and the fluid. The inward propagating waves depend on the solution exterior to the subdomains and therefore are computed from the boundary conditions, while the behavior of the outward propagating waves is determined by the solution inside the subdomain. The approach, given in Carcione (1991), and adapted here for equations (1)–(11), involves the following equations for updating the field variables at the grid points defining the fluid-solid interface:

$$
\begin{aligned}
v_x^{(\mathrm{new})}(1) &= v_x^{(\mathrm{old})}(1),\\
v_z^{(\mathrm{new})} &= [Z_P(1)+Z_P(2)]^{-1}\Big[Z_P(2)v_z^{(\mathrm{old})}\\
&\quad + Z_P(1)v_z^{(\mathrm{old})}\sigma^{(\mathrm{old})}(1) - \sigma_{zz}^{(\mathrm{old})}(2)\Big],\\
\sigma^{(\mathrm{new})} &= \sigma_{zz}^{(\mathrm{new})} = \frac{Z_P(1)Z_P(2)}{Z_P(1)+Z_P(2)}\Big[v_z^{(\mathrm{old})}(1) - v_z^{(\mathrm{old})}(2)\\
&\quad + \frac{\sigma^{(\mathrm{old})}(1)}{Z_P(1)} + \frac{\sigma_{zz}^{(\mathrm{old})}(2)}{Z_P(2)}\Big],\\
e_1^{(\mathrm{new})}(1) &= e_1^{(\mathrm{old})}(1) + [\phi_1(1)/k(1)]\Big[\sigma^{(\mathrm{new})} - \sigma^{(\mathrm{old})}(1)\Big],\\
v_x^{(\mathrm{new})}(2) &= v_x^{(\mathrm{old})}(2) - \sigma_{xz}^{(\mathrm{old})}(2)/Z_S(2),\\
\sigma_{xz}^{(\mathrm{new})}(2) &= 0,\\
\sigma_{xx}^{(\mathrm{new})}(2) &= \sigma_{xx}^{(\mathrm{old})}(2) + \frac{k(2)-\mu(2)}{k(2)+\mu(2)}\Big[\sigma_{zz}^{(\mathrm{new})} - \sigma_{zz}^{(\mathrm{old})}(2)\Big],\\
e_1^{(\mathrm{new})}(2) &= e_1^{(\mathrm{old})}(2) + [\phi_1(2)/(k(2)\\
&\quad + \mu(2))][\sigma_{zz}^{(\mathrm{new})} - \sigma_{zz}^{(\mathrm{old})}(2)],\\
e_2^{(\mathrm{new})}(2) &= e_2^{(\mathrm{old})}(2) - [\phi_2(2)/(k(2)\\
&\quad + \mu(2))][\sigma_{zz}^{(\mathrm{new})} - \sigma_{zz}^{(\mathrm{old})}(2)],\\
e_3^{(\mathrm{new})}(2) &= e_3^{(\mathrm{old})}(2) - [\phi_2(2)/\mu(2)]\sigma_{xz}^{(\mathrm{old})}(2),
\end{aligned}
\tag{23}
$$

where $\phi_v = 1/\tau_\sigma^{(v)} - 1/\tau_\epsilon^{(v)}$, $Z_P(1) = \rho_1 V_{P_1}$, $Z_P(2) = \rho_2 V_{P_2}$, and $Z_S(2) = \rho_2 V_{S_2}$.

The upper boundary of subdomain 1 (the fluid) may satisfy free-surface or nonreflecting boundary conditions (Carcione, 1992a, 1994a,b). The free-surface boundary equations are

$$
\begin{aligned}
v_x^{(\mathrm{new})} &= v_x^{(\mathrm{old})},\\
v_z^{(\mathrm{new})} &= v_z^{(\mathrm{old})} - \sigma^{(\mathrm{old})}/Z_P,\\
\sigma^{(\mathrm{new})} &= 0,\\
e_1^{(\mathrm{new})} &= e_1^{(\mathrm{old})} - (\phi_1/k)\sigma^{(\mathrm{old})}.
\end{aligned}
\tag{24}
$$

The nonreflecting boundary equations are

$$v_z^{(\text{new})} = \frac{1}{2}\left(v_z^{(\text{old})} - \sigma^{(\text{old})}/Z_P\right),$$
$$\sigma^{(\text{new})} = \frac{1}{2}\left(\sigma^{(\text{old})} - Z_P v_z^{(\text{old})}\right),$$
$$e_1^{(\text{new})} = e_1^{(\text{old})} - [\phi_1/(2k)](\sigma^{(\text{old})} + Z_P v_z^{(\text{old})}), \quad (25)$$

The lower boundary of subdomain 2 (the solid) satisfies nonreflecting boundary conditions (Carcione, 1992a, 1994a,b)

$$v_x^{(\text{new})} = \frac{1}{2}\left(v_x^{(\text{old})} + \sigma_{xz}^{(\text{old})}/Z_S\right),$$
$$v_z^{(\text{new})} = \frac{1}{2}\left(v_z^{(\text{old})} + \sigma_{zz}^{(\text{old})}/Z_P\right),$$
$$\sigma_{xx}^{(\text{new})} = \sigma_{xx}^{(\text{old})} - \frac{[k(2)-\mu(2)]}{2[k(2)+\mu(2)]}\left(\sigma_{zz}^{(\text{old})} - Z_P v_z^{(\text{old})}\right),$$
$$\sigma_{zz}^{(\text{new})} = \frac{1}{2}\left(\sigma_{zz}^{(\text{old})} + Z_P v_z^{(\text{old})}\right),$$
$$\sigma_{xz}^{(\text{new})} = \frac{1}{2}\left(\sigma_{xz}^{(\text{old})} + Z_S v_x^{(\text{old})}\right),$$
$$e_1^{(\text{new})} = e_1^{(\text{old})} - [\phi_1/(2(k+\mu))]\left(\sigma_{zz}^{(\text{old})} - Z_P v_z^{(\text{old})}\right),$$
$$e_2^{(\text{new})} = e_2^{(\text{old})} + [\phi_2/(2(k+\mu))]\left(\sigma_{zz}^{(\text{old})} - Z_P v_z^{(\text{old})}\right),$$
$$e_3^{(\text{new})} = e_3^{(\text{old})} - [\phi_2/(2\mu)]\left(\sigma_{xz}^{(\text{old})} - Z_S v_x^{(\text{old})}\right). \quad (26)$$

(Note that to obtain the boundary equations for the opposite boundary, say, horizontal boundaries, the method requires the following substitutions: $z \to -z$, which implies $v_z \to -v_z$, $\sigma_{xz} \to -\sigma_{xz}$, and $e_3 \to -e_3$.)

In addition to the nonreflecting conditions, absorbing strips are used to further attenuate the wave field at nonphysical boundaries (Carcione, 1992a).

It is important to consider that the modeling algorithm is 2D. In this case, the amplitude decay of the interface waves with range differs from that of a point source in 3D media, resulting in the absence of the 3D geometrical spreading. However, this limitation does not affect the analysis of the anelastic effects.

REFLECTION AND TRANSMISSION COEFFICIENTS

The plane-wave theory (Aki and Richards, 1980; Carcione, 2001, p. 212–214), is used to compute the reflection and transmission coefficients of sea-floor interfaces where the sea-floor is modeled by a viscoelastic solid. Various cases are shown in Figure 1, from a stiff ocean floor Figures 1a and 1d to a soft ocean floor (Figure 1c), where by stiff we denote those solids for which the S-wave velocity is greater than the sound velocity in water. The properties of water are taken as $V_{P_1} = 1490$ m/s, $\rho_1 = 1040$ kg/m^3, and $Q_0 = 10\,000$. The unrelaxed velocities, density, and loss parameters are indicated. The solid and dashed lines correspond to the elastic and viscoelastic cases, respectively. Let us analyze the lossless case. For $V_P = 4000$ m/s, we recognize the P-wave and S-wave critical angles at 22° and 51°, respectively. The S-wave critical angle is equal to 90° when $V_P = 3105$ m/s because the shear-wave velocity equals the sound speed in water. Similarly, the P-wave critical angle disappears when the P-wave velocity of the sediment is less than the sound speed in water. When $V_P = 1490$ m/s, we observe a Brewster angle at 72°. This angle approaches zero when the impedance of the sediment equals the impedance of water. In the viscoelastic case, critical and Brewster angles are very rare (e.g., Borcherdt et al., 1986; Carcione, 2001, p. 110).

Figure 1d shows the P-wave transmission coefficient for propagation from the sediment to the ocean for the case shown in Figure 1a. The incident wave is inhomogeneous (i.e, the attenuation vector is perpendicular to the water-sediment interface) (Carcione, 2001, p. 207). This condition is required to satisfy Snell's (viscoelastic) law at the interface, because water is practically a lossless medium.

The Rayleigh-window phenomenon

We first apply the theory to a water-steel interface, whose reflection coefficient was measured experimentally by Becker and Richardson (1970). Their ultrasonic experiments were verified with an anelastic model in a later paper (Becker and Richardson, 1972), in particular the Rayleigh-window phenomenon that cannot be predicted by using reflection coefficients based on the elasticity theory (Brekhovskikh, 1960, p. 34). The problem has been investigated by Borcherdt et al. (1986), who found that the Rayleigh window should be observable in appropriate sets of wide-angle reflection data and that can be useful in estimating attenuation for various ocean-bottom reflectors.

The compressional and shear velocities of steel are $V_{P_2} = 5740$ m/s and $V_{S_2} = 3142$ m/s, and the density is $\rho = 7932$ kg/m^3. The quality factors at 10 MHz are $Q_0^{(1)} = 140$ and $Q_0^{(2)} = 80$. Figure 2 represents the P-wave reflection coefficient and phase, where the value corresponding to $Q_0^{(1)} = 40$ is also shown. Actually, the value of the frequency has no influence, since the reflection coefficient is computed at the peak frequency of the Zener mechanism. The main factor affecting the window is the shear-wave attenuation, and the shear velocity controls the angular location of the minimum. The amplitude reaches zero at $Q_0^{(2)} = 44$, and below this value there is a phase reversal.

Let us consider now the same phenomenon at the ocean bottom. The compressional and shear velocities of a stiff oceanic crust are $V_{P_2} = 4850$ m/s and $V_{S_2} = 2800$ m/s, the density is $\rho = 2600$ kg/m^3, and $Q_0^{(1)} = 1000$ (although this value has practically no influence). Figure 3 represents the P-wave reflection coefficient and phase, for different values of the shear-wave quality factor. The value of least reflection is slightly higher than 10. For this value, there is a phase reversal. Simulations, corresponding to this case, are presented below.

Comparison of numerical and analytical solutions

We test the numerical solution against the analytical solution for lossless media. The analytical solution for the fluid-solid plane interface in lossless media is obtained by the method of Cagniard–de Hoop (de Hoop and van der Hijden, 1983; Berg et al., 1994). Regarding the simulation, each grid, corresponding to the fluid and solid phases, has 243×81 points with a grid spacing of 10 m in the horizontal direction and a vertical size of 510 m. The source is a dilatational Ricker-type wavelet located at 300 m above the interface, and has a dominant frequency of

20 Hz. The receiver is located at 400 m from the source and 300 m from the interface. We consider the properties of water and stainless steel, which implies a high material contrast at the interface. The Runge-Kutta algorithm requires a time step of 0.5 ms to be stable (sediments require, in general, 1 ms and therefore fewer time steps). The numerical and analytical solutions are compared in Figure 4, where it is clear that the agreement is excellent for lossless media. Later, we further compare numerical and analytical solutions when illustrating the propagation of interface waves.

AVO ANALYSIS

In order to verify the performance of the domain-decomposition method in the viscoelastic case, we compute the reflection coefficient versus incidence angle (AVO) from synthetic data generated by the modeling algorithm. The technique has been used by Kindelan et al. (1989) for elastic media. It consists of the following procedure.

1) Generate a synthetic seismogram of the pressure field by using a dilatational point source in water. Place a line

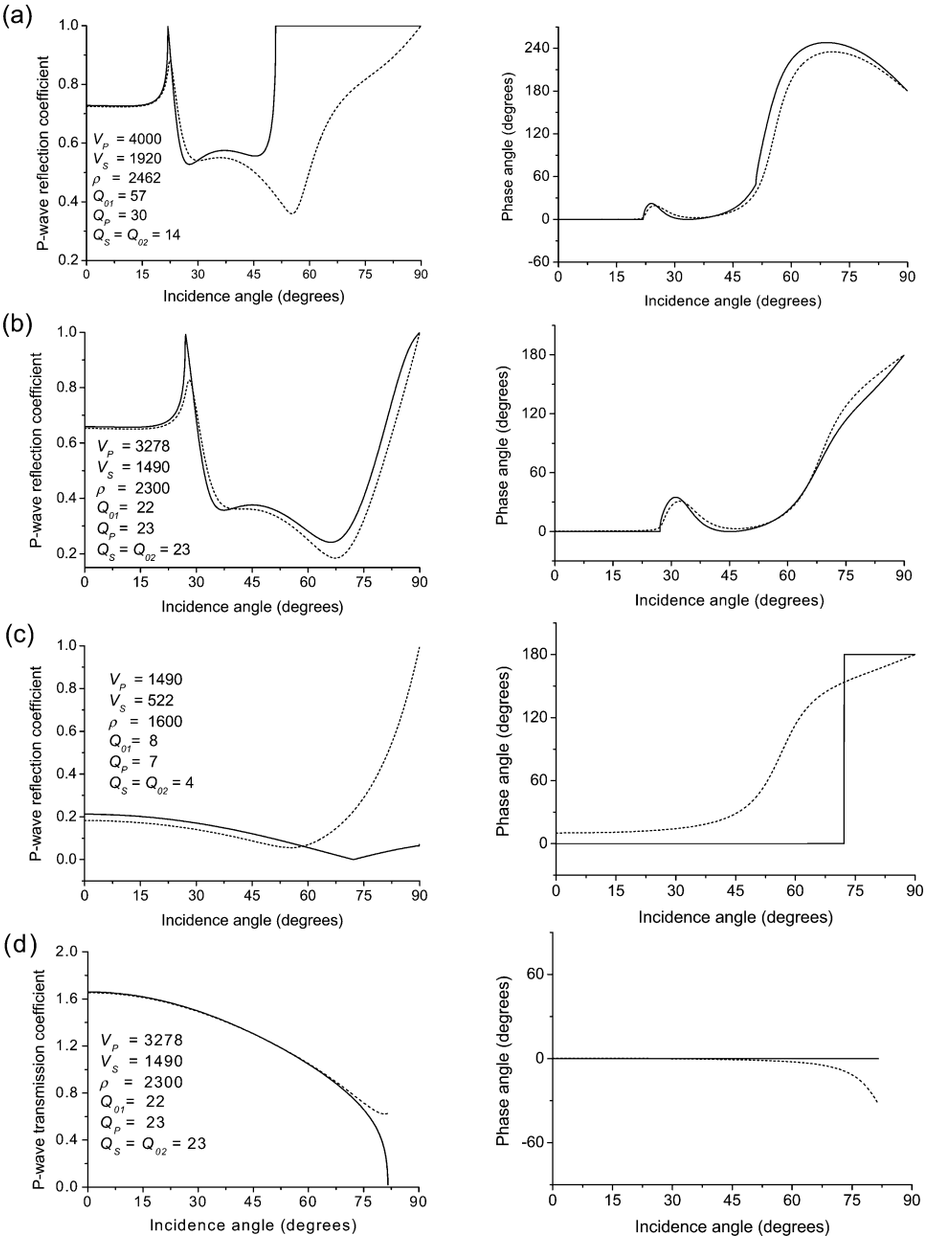

Figure 1. Water-ocean bottom interface. P-wave reflection coefficients and phase versus incidence angle for different material properties [from a stiff ocean floor (a) to a soft ocean floor (c)]. Panel (d) shows the P-wave transmission coefficients and phase versus incidence angle for waves traveling from the ocean crust to the ocean (the incident wave is inhomogeneous in this case). The unrelaxed velocities, density, and loss parameters are indicated. The solid and dashed lines correspond to the elastic and viscoelastic cases, respectively. Units are in the SI system.

of receivers at each grid point above the interface. This record contains the incident and reflected fields.

2) Compute the synthetic seismogram without interface (without ocean bottom) at the same location. The seismogram contains the incident field only.
3) Perform the difference between the first and second seismograms. The difference contains the reflected field only.
4) Perform an (ω, k_x)-transform of the incident field to obtain $\sigma_0(\omega, k_x)$.
5) Perform an (ω, k_x)-transform of the reflected field to obtain $\sigma(\omega, k_x)$.
6) The ratio $|\sigma(\omega, k_x)|/|\sigma_0(\omega, k_x)|$ is the reflection coefficient.
7) The phase angle is given by $\arctan[\sigma(\omega, k_x)/\sigma_0(\omega, k_x)]$. Transform k_x to incidence angle by using $\sin\theta = V_{P_1} k_x/\omega$.

We consider a stiff ocean bottom, whose reflection coefficient is shown in the top picture of Figure 1. The modeling parameters are those of the previous simulation, allowing a maximum incidence angle of approximately 70°. Beyond this angle, the traces are tapered by the absorbing boundary. Therefore, there is no need of tapering to compute the Fourier transform to the wavenumber domain. Receivers (hydrophones) are located 1.2739 m above the ocean bottom. The time step is 0.5 ms, and we store the traces with a sampling rate of 8 ms. Figure 5 shows the comparison between the elastic (a) and viscoelastic (b) reflection coefficients. The symbols correspond to the numerical evaluation for different frequencies (triangle: 28 Hz; circle: 29 Hz; star: 30 Hz). In general, the use of high frequencies yields a better result (the source central frequency is 20 Hz). This comparison confirms the good performance of the domain-decomposition method to model fluid-solid interfaces when there is attenuation, i.e., it provides a test of the boundary equations related to the memory variables [see equation (23)]. Moreover, as can be seen in Figure 5a, the method works very well at critical angles.

Let us consider the Rayleigh-window problem. Figure 6 and 7 show the numerical evaluation of the P-wave reflection coefficient (a) and phase angle (b) for the oceanic crust, defined by $V_{P_2} = 4850$ m/s, $V_{S_2} = 2800$ m/s, $\rho = 2600$ kg/m^3, $Q_0^{(1)} = 1000$, $Q_0^{(2)} = 10$ (Figure 6, dotted line in Figure 3), and $Q_0^{(2)} = 7$ (Figure 7) As can be observed, the modeling algorithm

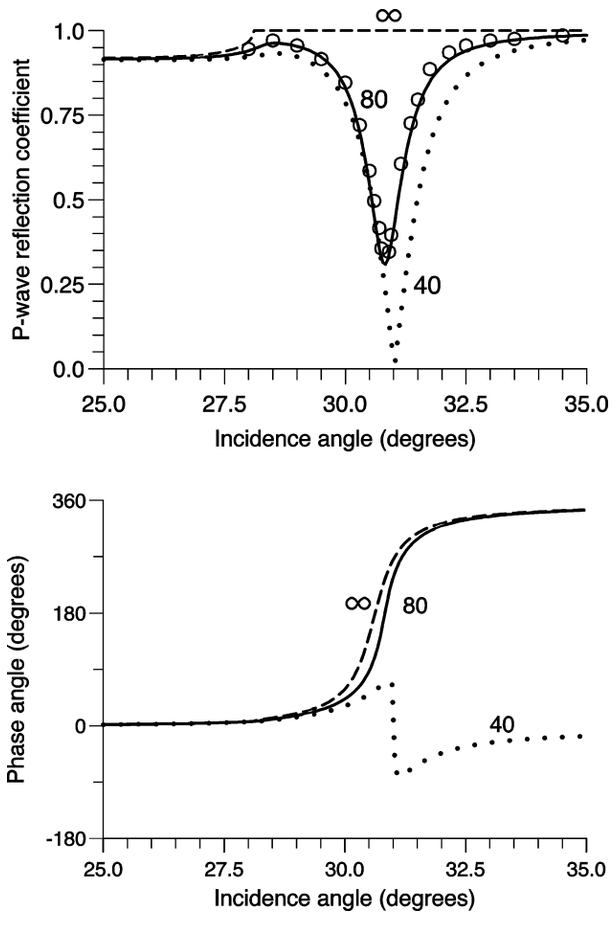

Figure 2. Water–stainless steel interface. P-wave reflection coefficient and phase versus incidence angle for different values of the shear-wave quality factor $Q_0^{(2)}$. The phase reversal at the Rayleigh angle occurs when $Q_0^{(2)} < 44$. This value corresponds to a zero reflection coefficient at the Rayleigh angle.

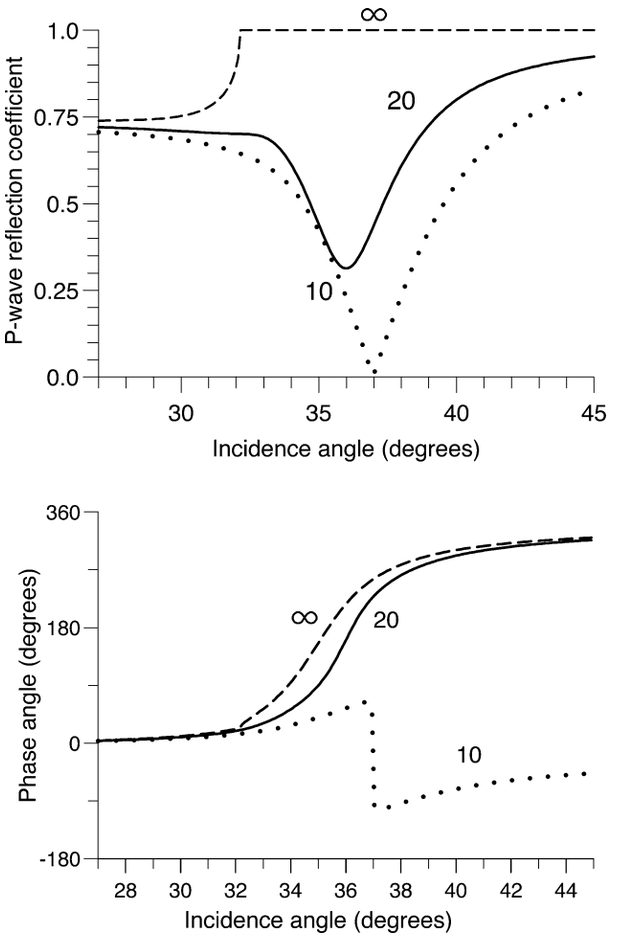

Figure 3. Stiff ocean-crust interface. P-wave reflection coefficient and phase versus incidence angle for different values of the shear-wave quality factor $Q_0^{(2)}$. The phase reversal at the Rayleigh angle occurs when $Q_0^{(2)} \leq 10$. This value corresponds to a zero reflection coefficient at the Rayleigh angle.

correctly simulates the Rayleigh window phenomenon (i.e., the magnitude of the reflection coefficient and phase-change slope). The mismatch between theory and numerical experiments is due to the fact that the receivers are located at h = 1.2739 m above the interface. Also, there is a phase shift between the incident wave and the reflected wave. At normal incidence, the correction is $\arctan(2h\omega/V_{P_1})$. For a frequency of $f = 20$ Hz and $V_{P_1} = 1480$ m/s, we obtain 12°, which coincides with the mismatch observed in Figure 6.

It is difficult to observe the Rayleigh-wave phenomenon in the space-time domain, since the reflected pulse is masked by the head wave, because the window is located beyond the critical angle. The results of Figures 6 and 7 (i.e., the perfect agreement between analytical and numerical results) constitute a further confirmation of the correctness of the modeling method. To our knowledge, this is the first simulation of this phenomenon by using direct grid methods. Schmidt and Jensen (1985) simulated the Rayleigh window, but they used a wavenumber-domain algorithm for plane layers, similar to the Thomson-Haskell technique (Ewing et al., 1957, p. 124).

SCHOLTE AND LEAKY RAYLEIGH WAVES

Interface waves at liquid-solid boundaries have been investigated with some detail in the field of nondestructive testing of materials, where the experiments are performed in the ultrasonic range. The research performed in this field is relevant for seismic exploration and geotechnical applications. We consider the two interfaces given in Table 1. The velocities of the Scholte wave ($V_{\rm SCH}$) and leaky Rayleigh wave ($V_{\rm RL}$) are indicated. The first wave correspond to the choice (+, +, +) for the signs of $\sqrt{1-q}$, $\sqrt{1-aq}$, and $\sqrt{1-bq}$; the second surface wave corresponds to a lower sheet with the choice (+, −, +). Roots in lower sheets, such as (1878, −24) m/s and (2097,97) m/s are physically impermissible steady-state waves, but the result of superposition in the time domain may be physically reasonable (Phinney, 1961).

Table 1. Properties of fluid, solid and surface waves.

Interface	V_{P_1} (m/s)	ρ_1 (kg/m^3)	V_{P_2} (m/s)	V_{S_2} (m/s)	ρ_2 (kg/m^3)	$V_{\rm SCH}$ (m/s)	$V_{\rm LR}$ (m/s)
Water-Plexiglas[1]	1480	1000	2745	1390	1180	1058	1363
Water-glass[2]	1500	1000	5712	3356	2500	1496	3091

[1] Padilla et al. (1999).
[2] Glorieux et al. (2002).

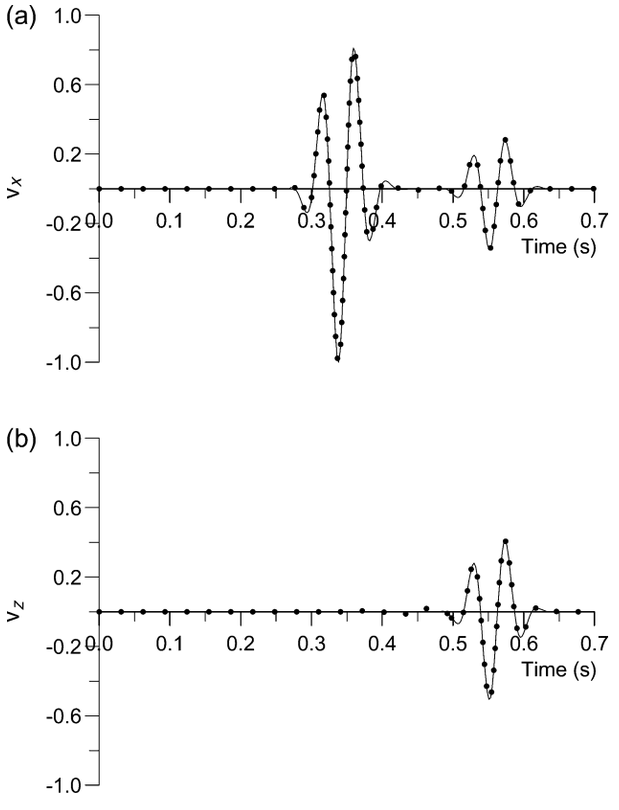

Figure 4. Numerical and analytical solutions (dots and solid line, respectively) of the v_x-component (a) and v_z-component (b) corresponding to the water–stainless steel interface. The first event is the direct wave and the second event is the reflected wave.

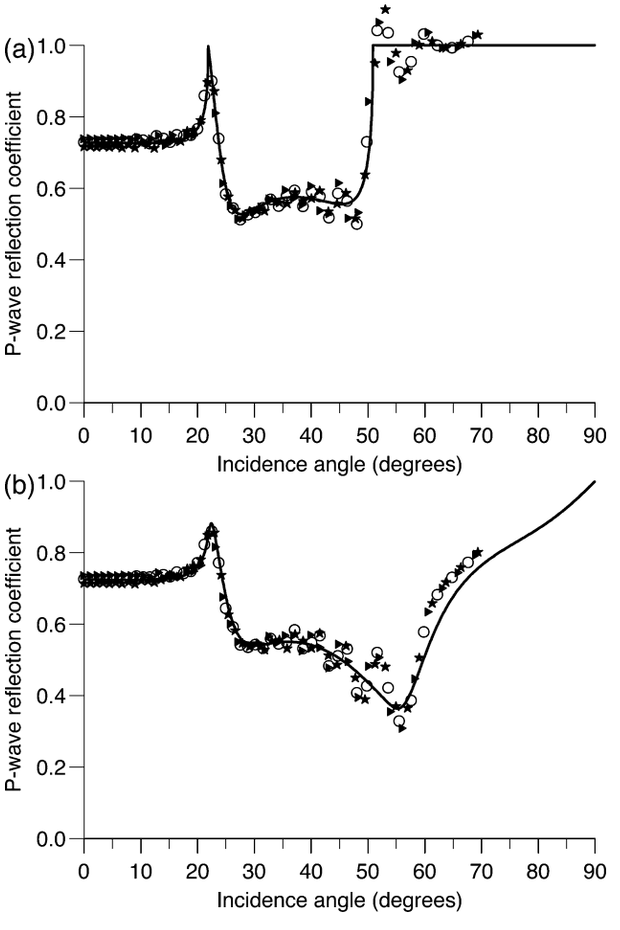

Figure 5. Stiff ocean-crust interface. Elastic (a) and viscoelastic (b) P-wave reflection coefficients versus incidence angle for case (a) of Figure 1. The symbols correspond to the numerical evaluation for different frequencies (triangle: 28 Hz; circle: 29 Hz; star: 30 Hz).

As shown by Glorieux et al. (2002) from laboratory experiments and by our simulations (see below), the real solution $V_{SCH} = 1363$ m/s is not a physical solution, which has been identified by Padilla et al. (1999) as an unleaky Rayleigh wave. On the other hand, the corresponding solution for the water-glass interface is a complex physical solution with value (3091,−109) m/s.

Numerical simulations

Let us consider the simulation of wave propagation. Each grid has 405×81 points with a horizontal grid spacing of 0.5 mm and a vertical size of 30 mm. The source is a dilatational force applied to the surface of the solid, with a dominant frequency of 500 kHz. Forty grid points are used as absorbing boundary at the sides, top, and bottom of the grids. The time step is 40 ns for water-Plexiglas and 20 ns for water-glass.

Figure 8 shows a snapshot at 40 μs (a) and synthetic traces of the vertical particle-velocity component at the interface (b), corresponding to the water-Plexiglas interface. The Scholte wave is the dominant event (this wave has been clipped in the snapshot). The P wave in the liquid (1480 m/s) and the shear wave in the solid (1390 m/s) can also be appreciated. We have not seen the surface Rayleigh wave (1363 m/s) observed by Padilla et al. (1999) in their ultrasonic experiments. The Scholte-wave energy is localized closer to the interface [see plots of the displacement in Figure 5 of Glorieux et al. (2002)].

The results of the water-glass interface are shown in Figure 9. The two head waves connect the P wavefront in the liquid with the S and P wavefronts in the solid. The Scholte and leaky Rayleigh waves show their characteristic elliptical wave motion. The leaky Rayleigh wave and the shear body wave can hardly be separated in the synthetic traces. Evidence of the leaky wave is given by Luke and Stokoe (1998), who performed laboratory experiments on a slab of concrete. (They also show a field test in the Gulf of Mexico, where the Scholte wave is the dominant event.) Plots of the normal displacement by Glorieux et al. (2002) indicate that most of the Scholte wave energy is localized in the liquid and that this wave behaves as a plane bulk wave traveling in the liquid along the interface. This behavior is called weak localization and occurs when the solid is

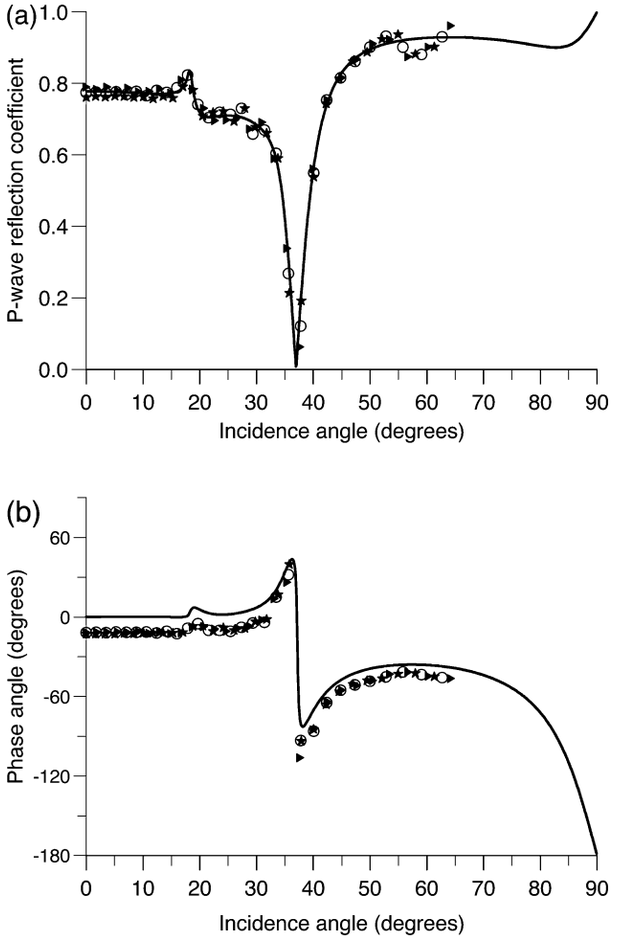

Figure 6. The Rayleigh window at a stiff ocean-crust interface [$Q_0^{(2)} = 10$ (dotted line in Figure 3)]. P-wave reflection coefficient (a) and phase angle (b) versus incidence angle. The symbols correspond to the numerical evaluation of the AVO response at different frequencies (triangle: 18 Hz; circle: 19 Hz; star: 20 Hz).

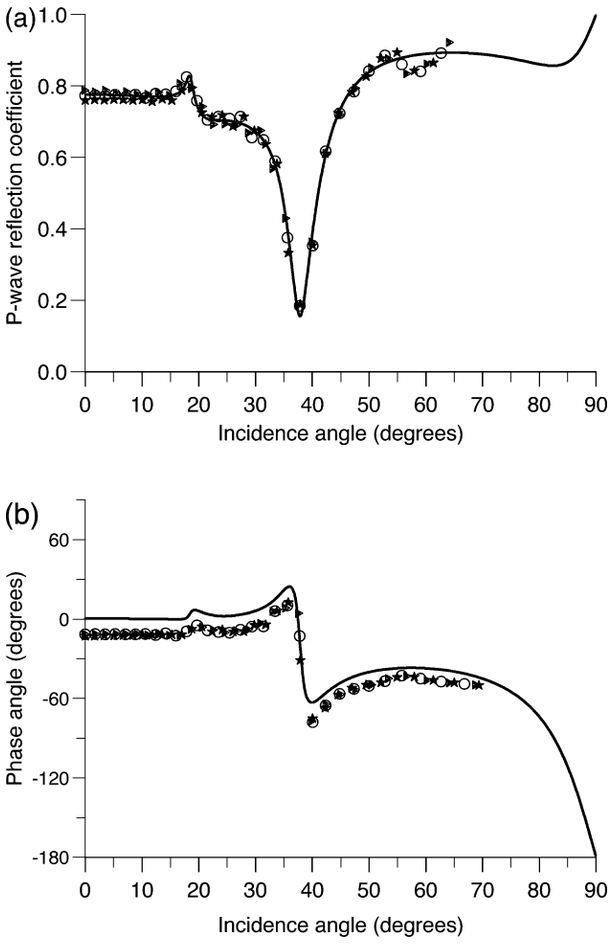

Figure 7. The Rayleigh window at a stiff ocean-crust interface ($Q_0^{(2)} = 7$). P-wave reflection coefficient (a) and phase angle (b) versus incidence angle. The symbols correspond to the numerical evaluation of the AVO response at different frequencies (triangle: 18 Hz; circle: 19 Hz; star: 20 Hz).

much harder than the liquid. In these cases, the inversion of the shear-wave velocity is not possible because the Scholte wave is not sensitive to the properties of the solid. The inversion is feasible for soft materials. The energy of the leaky Rayleigh wave is radiated into the liquid as a P-wave, under the Rayleigh angle [64° with respect to the interface; see the strong head wave in Figure 9a, the attenuation with increasing distance in Figure 9b, and Figure 3 of Glorieux et al. (2002)].

Figure 10 shows comparisons of the numerical and analytical solutions, corresponding to the water-Plexiglas interface (a and b) and water-glass interface (c and d). The source-receiver configuration is the same as for the previous numerical experiment. The agreement between solutions is very good. These comparisons confirm the accuracy of the modeling algorithm and verify the previous physical interpretations. We have not seen the Rayleigh wave observed by Padilla et al. (1999) in the analytical solution corresponding to the water-Plexiglas interface. There are two waves with approximately the same traveltime of the hypothetical leaky Rayleigh wave. These waves travel with the velocity of the P-wave in the liquid and the velocity of the S-wave in the solid. Since the receiver is located in the solid at 38.4 μm from the interface, the first wave could be the head wave described by Brekhovskikh (1960) as a $P_1P_2S_2$ event, and simulated by Stephen and Bolmer (1985) (see their Figure 4).

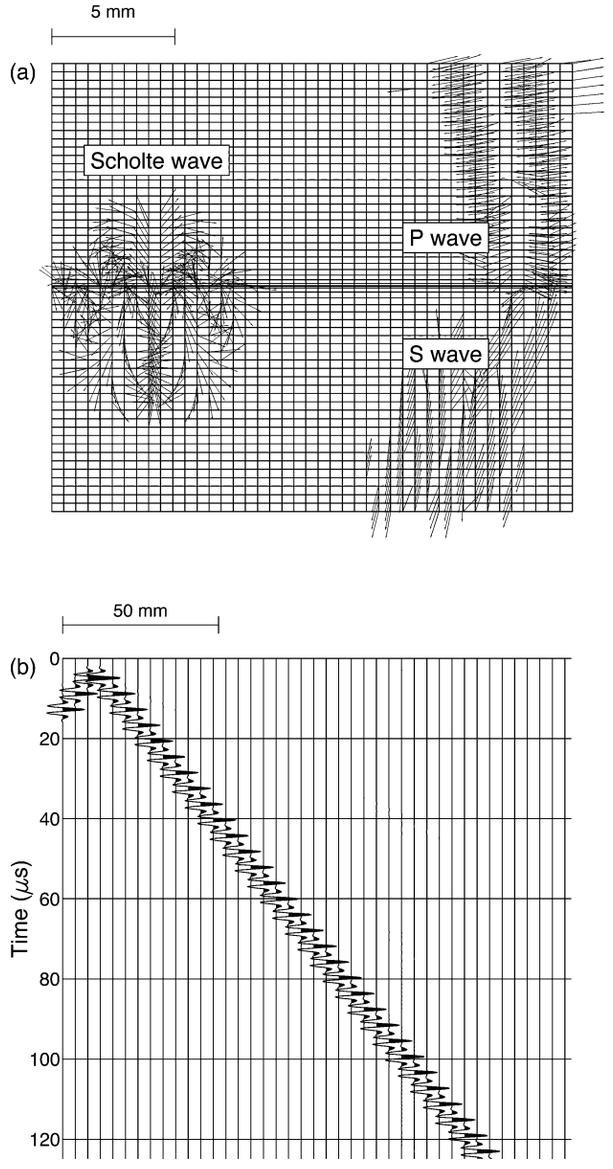

Figure 8. Snapshot at 40 μs (a) and synthetic traces of the vertical particle-velocity component recorded at the interface (b), corresponding to the water-Plexiglas interface. The Scholte wave is the dominant event (this wave has been clipped in the snapshot).

Acoustic properties: Velocity and attenuation.

Figure 11 shows the Scholte-wave phase velocity and quality factor versus P-wave velocity, S-wave velocity, and density of the solid phase. Panels (a)–(c) corresponds to a stiff bottom and panels (d)–(f) to a soft bottom (see Figure 1). Phase velocity and quality factor are calculated by using equations (18) and (20), respectively, where v is the Scholte-wave complex velocity. The quality factor associated with the P-wave is given by $Q_P = 5Z_P = 5\rho[\mathrm{g/cm^3}]V_P[\mathrm{km/s}]$ [this equation is based on

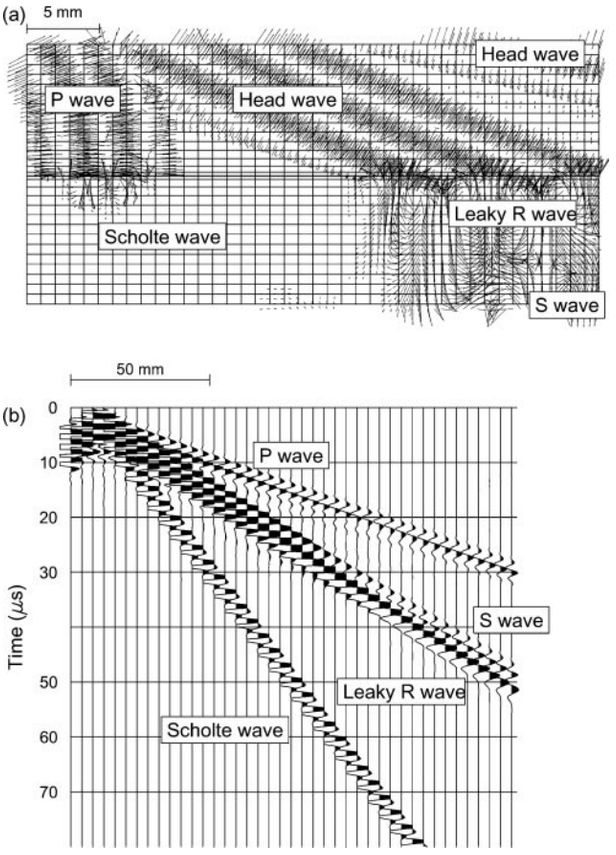

Figure 9. Snapshot at 20 μs (a) and synthetic traces of the vertical particle-velocity component recorded at the interface (b), corresponding to the water-glass interface. The Scholte wave is weaker than in the previous case (see Figure 8).

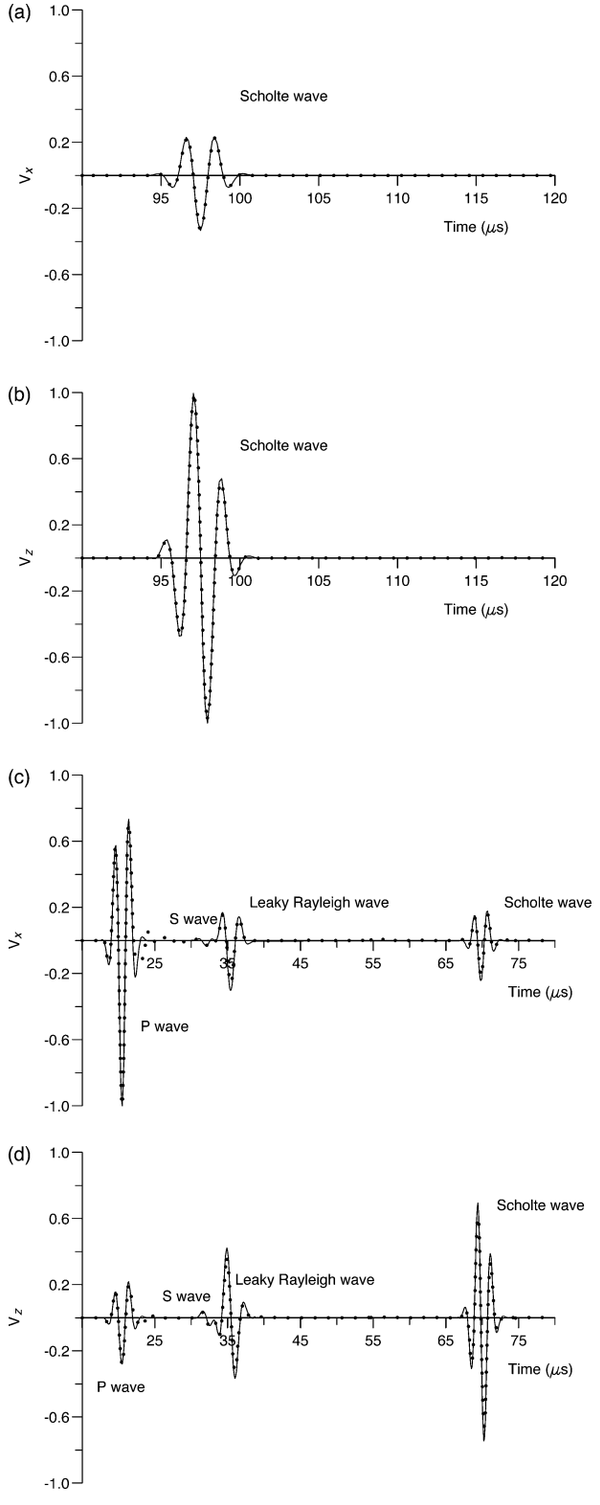

Figure 10. Numerical and analytical solutions (dots and solid line, respectively) of the v_x-component (a and c) and v_z-component (b and d), corresponding to the water-Plexiglas interface (a and b) and water-glass interface (c and d). The source is a compressional wave applied to the solid at 38.4 μm from the interface. The receiver is located at the same position and at 100 mm from the source. The different waves are indicated.

data published by Prasad (1998)], and the quality factor associated with the S-wave is given by $Q_S = 2Q_P(V_S/V_P)^2$ (Hamilton, 1976).

The velocities are derived from the empirical results published by Hamilton (1972, 1976, 1979) and Hamilton and Bachman (1982). The velocity of the Scholte wave tends to the fluid velocity for increasing shear-wave velocity (stiff sediments). At high values of V_S, it is practically constant, precluding the inversion of the shear-wave parameters. Also, for soft sediments, the phase velocity is sensitive to variations of V_P, but shows a strong dependence on V_S, which offers an opportunity of inverting for S-wave variations along the seabed as shown by Stoll et al. (1994). The quality factor for the Scholte wave is generally higher than the shear-wave quality factor. For soft sediments, the quality factors are significantly lower than for stiff sediments.

Figure 12 shows the phase velocity and quality factor of the leaky Rayleigh wave versus P-wave velocity, S-wave velocity,

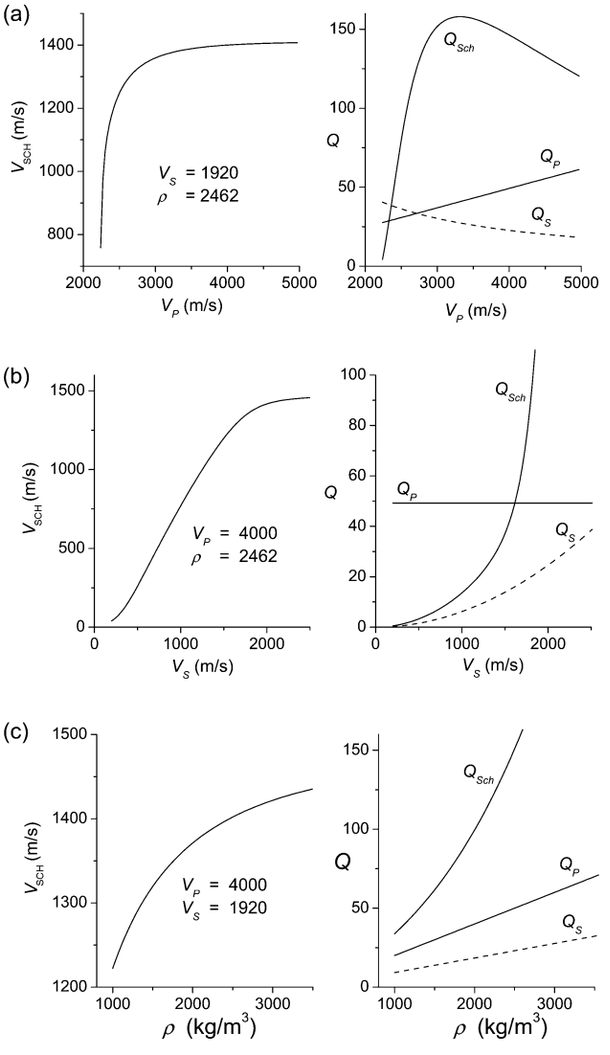

Figure 11. Scholte-wave phase velocity and quality factor versus P-wave velocity, S-wave velocity, and density of the ocean bottom. Panels (a)–(c) corresponds to a stiff bottom and panels (d)–(f) to a soft bottom (see Figure 1). Units are in the SI system. (*Continued*).

and density of the solid for the same model discussed in Figure 11a (stiff bottom, i.e., $V_{P_1} < V_S$). In contrast to the free Rayleigh wave, the leaky Rayleigh wave does not exist for all liquid-solid interfaces. With increasing P-wave velocity, the leaky Rayleigh wave velocity and quality factor tend to those of the S-wave. The dependence with the S-wave velocity is practically linear, whereas a decrease in velocity versus density is evident, tending towards the velocity of the Rayleigh wave for the vacuum-solid interface as the density ratio ρ_1/ρ_2 decreases. The quality factor is, in general, lower than the shear-wave quality factor.

SIMULATION OF A REAL SEISMOGRAM: DISPERSIVE INTERFACE WAVES

The modeling algorithm allows us to investigate cases of complex geology, which apply to the propagation of earthquake surface waves across the ocean and to geophysical prospecting offshore. The physics is characterized by the propagation of infinite modes, showing velocity dispersion (e.g., Biot, 1952; Ewing et al., 1957, p. 156, 178, 224). We consider a shear-wave velocity profile of North Sea ocean-bottom sediments obtained by Allnor et al. (1997) by analyzing Scholte waves (see also Muyzert, 2000). The data corresponds to the Tommeliten field (Granli et al., 1999), where a sensor array was planted at the sea floor. The profile is shown in Table 2, where the other parameters are obtained from empirical results published by Hamilton (1972, 1976, 1979) and Hamilton and Bachman (1982). The resulting values of the shear-wave quality factor agree with those reported by Dorman et al. (1991), Bromirski et al. (1992), and Nolet and Dorman (1996). The meshes have 405×17 and 405×81 grid points (water and sediments, respectively). The horizontal grid spacing is 5 m and the vertical size is 70 m for the upper mesh (water depth), and 510 m for the lower mesh (sediments). The source is located at 13 m below the sea surface and has a dominant frequency of 15 Hz. The upper mesh satisfies the free-surface boundary conditions (24) at the first row of grid points, while 40 grid points are used as absorbing boundary at the sides of both meshes and bottom of the lower mesh [in addition to the nonreflecting conditions (25)]. The time step of the Runge-Kutta method is 1 ms.

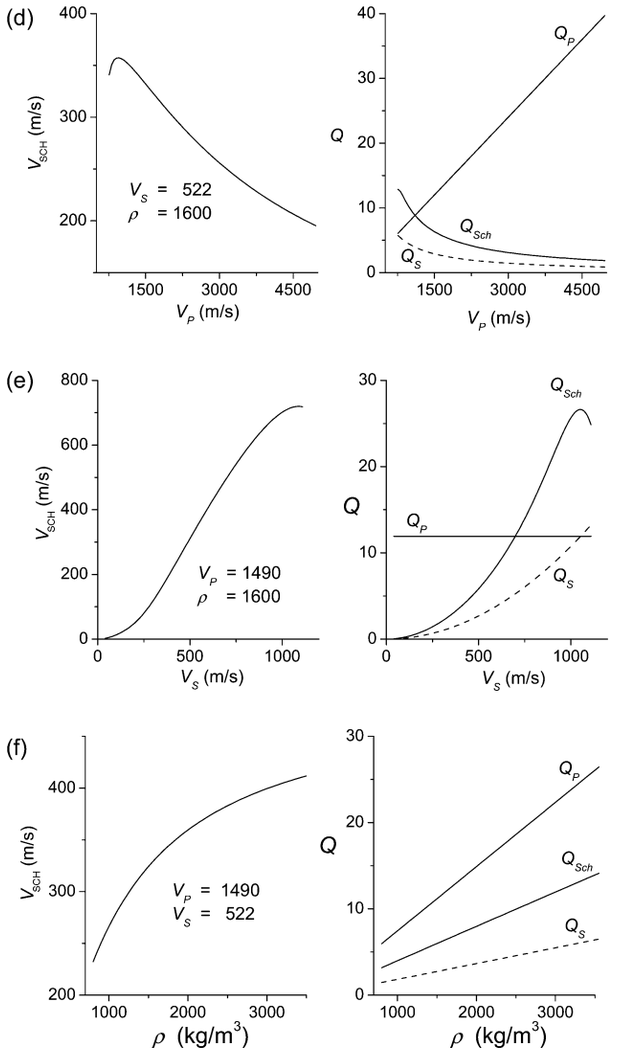

Figure 11. (*Continued*).

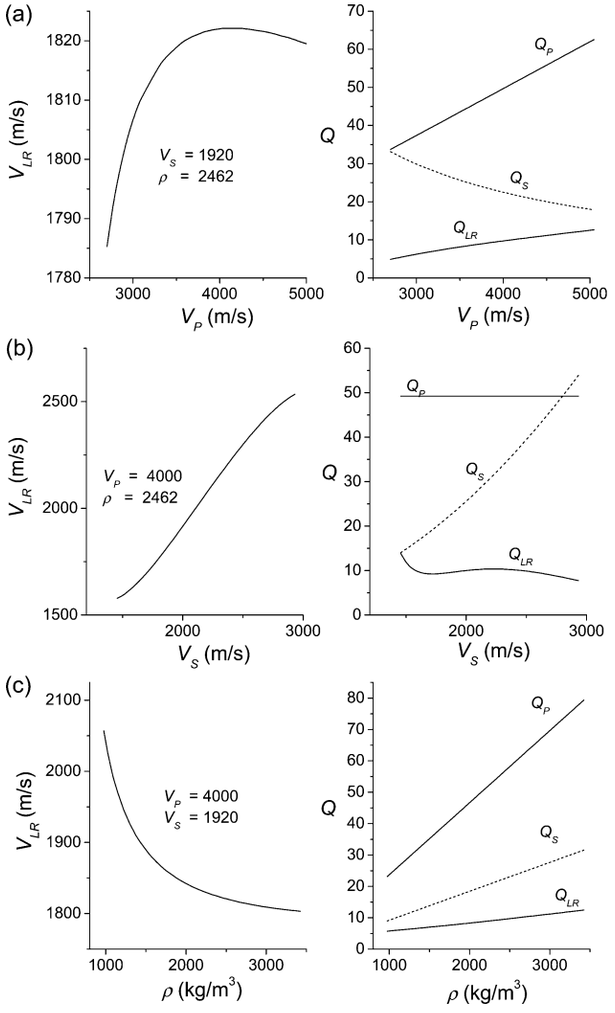

Figure 12. Phase velocity and quality factor of the leaky Rayleigh wave versus P-wave velocity, S-wave velocity, and density of the ocean bottom. Units are in the SI system.

Figure 13 shows synthetic seismograms of the horizontal particle-velocity component recorded at the ocean bottom for the lossless (Figure 13a) and lossy (Figure 13b) cases. Three modes can be seen: the fundamental mode M0, the first higher mode M1, and second higher mode M2, using the notation of Muyzert (2000). A quadratic gain versus time has been applied to the seismogram (in Figure 13b). The fundamental mode is highly affected by anelasticity. This is the case in the real seismogram, where mode M0 is weaker than modes M1 and M2. Another feature is that the slope of M0 in Figure 13b agrees with that of the real seismogram, while arrival times of this event in the lossless seismogram are quite different from the real ones. A proper analysis of the physics of dispersive modes requires energy considerations because the kinematic concept of group velocity loses its physical meaning in anelastic media (e.g., Carcione, 1992b).

CONCLUSIONS

We have investigated the physics of wave propagation at the ocean bottom, mainly the phenomena related to the anelastic effects. The analysis has required the improvement of the pseudospectral method to model the interface boundary condition between the ocean and the sea-bottom sediments (or ocean crust). The new features of the modeling method involve the inclusion of viscoelastic dissipation and the use of a domain decomposition technique. The high accuracy of the modeling has been verified by using the analytical solution for a fluid-elastic solid plane boundary, and the theory of reflection of plane waves at a fluid-viscoelastic solid interface. The modeling allows for the presence of the sea surface and general material variability along the vertical and horizontal directions.

The following phenomena regarding the physics have been analyzed:

1) Reflection and transmission coefficients and comparison with the lossy case. The various cases go from a stiff ocean floor, characterized by critical angles, to a soft ocean floor, characterized by a Brewster angle (this angle disappears when the impedance of the sediment is lower than the impedance of water). In the lossy case, critical and Brewster angles are the exception.
2) The anelastic effects on the reflection coefficients (amplitude and phase), verified by using an AVO analysis that can be used to process ocean-bottom cable data. Tests on synthetic data serve to verify the modeling of the anelastic effects and shows the accuracy of the AVO analysis.
3) The first simulation of the Rayleigh-window phenomenon with a direct grid method. This phenomenon can be used to obtain information about the shear-wave velocity and quality factor of the ocean bottom.
4) Simulation of Scholte and leaky Rayleigh waves. Confirmation that the first type of event is dominant in soft sediments and the second event is comparable in amplitude to the first in stiff ocean bottoms. The simulations

Table 2. Properties of the ocean bottom (North Sea sediments).

Layer	Depth (m)	V_P (m/s)	V_S (m/s)	ρ (kg/m^3)	Q_P	$Q_S(Q_0^{(2)})$	$Q_0^{(1)}$
1	0–12	1530	200	1467	34	14	35
2	12–22	1575	300	1551	37	33	37
3	22–33	1590	340	1578	38	43	37
4	33–39	1650	375	1684	42	54	41
5	39–71	1700	390	1768	45	59	44
6	71–98	1750	450	1847	48	80	47
7	98–132	1810	475	1938	53	91	50
8	132–160	1840	500	1981	55	101	52
9	160–∞	1930	560	2102	61	128	57

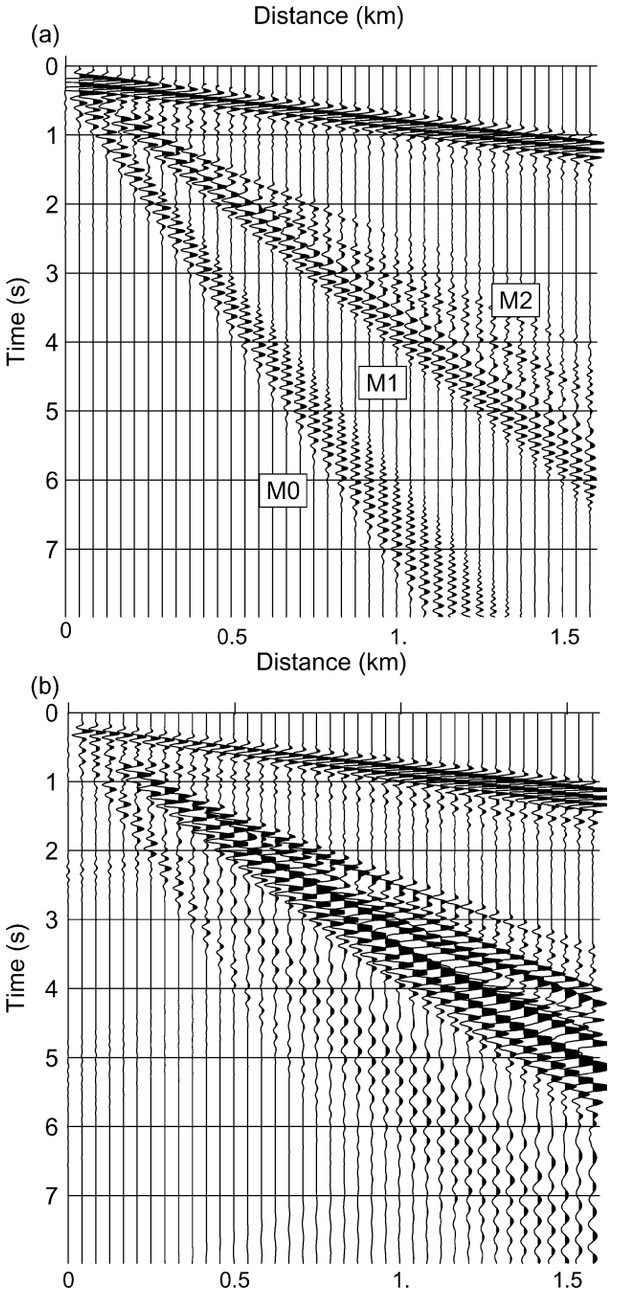

Figure 13. Synthetic seismograms of the horizontal particle-velocity component at the ocean bottom for the lossless (a) and lossy (b) cases. Three modes can be seen: the fundamental mode M0, the first higher mode M1, and second higher mode M2. A quadratic gain versus time has been applied to seismogram (b).

verify the absence of a free Rayleigh mode when the value of the shear-wave velocity is less than the sound velocity of the fluid.

5) The modeling has been used to compute synthetic seismograms at a North Sea site, showing the different dispersive modes recorded at the ocean bottom in the lossless and lossy cases. The fundamental mode is highly affected by anelasticity.

Use of this type of modeling to estimate the anelastic properties of the sea floor requires a theoretical analysis of the influence of attenuation on the phase and energy velocities and the quality factors of the different modes (group velocity loses its physical meaning in anelastic media, and the analysis should be based on the energy densities and Umov-Poynting vector). Ongoing research includes the analysis of the physics (scattering coefficients, Rayleigh window, interface waves) for a heterogeneous anelastic ocean bottom and the extension of the modeling algorithm to the 3D case and anisotropic media to model fine-layering and compaction effects.

ACKNOWLEDGMENTS

This work was supported by Norsk Hydro a.s. (Bergen). We are grateful to Børge Arntsen, three anonymous reviewers, and the editor for useful comments that improved the paper.

REFERENCES

Aki, K., and Richards, P. G., 1980, Quantitative seismology: W. H. Freeman and Co.

Allnor, R., Caiti, A., Arntsen, B., 1997, Inversion of seismic surface waves for shear wave velocities: 67th Annual Internation Meeting, SEG, Expanded Abstracts, 1921–1923.

Ansell, J. H., 1972, The roots of the Stoneley wave equation for liquid-solid interfaces: Pure and Applied Geophysics, **94**, 172–188.

Ash, E. A., and Paige, E. G. S. eds., 1985, Rayleigh-wave theory and application: Springer-Verlag.

Auld, B. A., 1985, Rayleigh wave propagation, *in* Ash, E. A., and Paige, E. G. S. eds., Rayleigh-wave theory and application: Springer-Verlag, 12–27.

Becker, F. L., and Richardson, R. L., 1970, Ultrasonic critical angle reflectivity, in R. S. Sharpe, ed., Research techniques in nondestructive testing: Academic Press, 91–131.

——— 1972, Influence of material properties on Rayleigh critical-angle reflectivity: Journal of the Acoustic Society of America, **51**, 1609–1617.

Berg, P., If, F., Nielsen, P., and Skovgaard, O., 1994, Analytical reference solutions, *in* K. Helbig, ed., Modeling the earth for oil exploration: Pergamon Press, 421–427.

Berteussen, K. A., and Alstad, O. J., 1985, Estimation of seabottom reflection characteristics and source signature from seabed reflected waves: Geophysics, **50**, 1049–1060.

Biot, M. A., 1952, The interaction of Rayleigh and Stoneley waves in the ocean bottom: Bulletin of the Seismic Society of America, **42**, 81–93.

Bohlen, T., Klein, G., Duveneck, E., Milkereit, B., and Franke, D., 1999, Analysis of dispersive seismic surface waves in submarine permafrost: 61st Annual Meeting, European Association of Exploration Geophysicists, Expanded Abstracts, paper 6–37.

Borcherdt, R. D., Glassmoyer, G., and Wennerberg, L., 1986, Influence of welded boundaries in anelastic media on energy flow, and characteristics of *P*, *S*-I and *S*-II waves: Observational evidence for inhomogeneous body waves in low-loss solids: Journal of Geophysical Research, **91**, 11 503–11 118.

Brekhovskikh, L. M., 1960, Waves in layered media: Academic Press.

Brekhovskikh, L. M., and Lysanov, Y. P., 1991, Fundamentals of ocean acoustics: Springer-Verlag.

Bromirski, P. D., Frazer, L. N., and Duennebier, F. K., 1992, Sediment shear *Q* from airgun OBS data: **110**, 465–485.

Brower, N. G., Himberger, D. E., and Mayer, W. G., 1979, Restrictions on the existence of leaky Rayleigh waves: IEEE Transactions on Sonics and Ultrasonics, **SU-26**, 306–308.

Cagniard, L., 1962, Reflection and refraction of progressive seismic waves: McGraw-Hill Book Co., Inc.

Carcione, J. M., 1991, Domain decomposition for wave propagation problems: Journal of Scientific Computing, **6**, 453–472.

——— 1992a, Modeling anelastic singular surface waves in the earth: Geophysics, **57**, 781–792.

——— 1992b, Rayleigh waves in isotropic-viscoelastic media: Geophysical Journal International, **108**, 453–464. (Erratum: 1992, **111**, 191).

——— 1994a, Time-dependent boundary conditions for the 2D linear anisotropic-viscoelastic wave equation: Numerical Methods for Partial Differential Equations, **10**, 771–791.

——— 1994b, The wave equation in generalized coordinates: Geophysics, **59**, 1911–1919.

——— 1996, A 2-D Chebyshev differential operator for the elastic wave equation: Computational Methods for Applied Mechanical Engineering, **130**, 33–45.

——— 2001, Wave fields in real media. Theory and numerical simulation of wave propagation in anisotropic, anelastic and porous media: Pergamon Press.

Carcione, J. M., Herman, G., and ten Kroode, F. P. E., 2002, Seismic modeling: Geophysics, **67**, 1304–1325.

Chamuel, J. R., 1991, Laboratory studies of pulsed leaky Rayleigh wave components in a water layer over a solid bottom, *in*, J. M. Hovem, M. D. Richardson, and R. D. Stoll, eds., Shear waves in marine sediments, Kluwer Academic Publishers, 59–66.

Christensen, R. M., 1982, Theory of viscoelasticity: Academic Press Inc.

de Hoop, A. T., and van der Hijden, J. H. M. T., 1983, Generation of acoustic waves by an impulsive line source in a fluid/solid configuration with a plane boundary: Journal of the Acoustic Society of America, **74**, 333–342.

Dorman, L. M., Schreiner, A. E., and Bibee, L. D., 1991, The effects of shear velocity structure on seafloor noise, *in*, J. M. Hovem, M. D. Richardson, and R. D. Stoll, eds., Shear waves in marine sediments, Kluwer Academic Publishers, 239–245.

Edelman, I., and Wilmanski, K., 2002, Asymptotic analysis of surface waves at vacuum/porous medium and liquid/porous medium interfaces: Continuum Mechanics and Thermodynamics, **14**, 25–44.

Ergin, K., 1952, Energy ratio of the seismic wave reflected and refracted at a rock-water boundary: Bulletin of the Seismic Society of America, **42**, 349–372.

Ewing, W. M., Jardetzky, W. S., and Press, F., 1957, Elastic waves in layered earth: McGraw-Hill Book Co., Inc.

Farnell, G. W., 1970, Properties of elastic surface waves: Academic Pres.

Favretto-Anrès, N., 1996, Theoretical study of the Stoneley-Scholte wave at the interface between an ideal fluid and a viscoelastic solid: Acustica, **82**, 829–838.

Favretto-Anrès, N., and Rabau, G., 1997, Excitation of the Stoneley-Scholte wave at the boundary between an ideal fluid and a viscoelastic fluid: Journal of Sound and Vibration, **203**, 193–208.

Favretto-Anrès, N., and Sessarego, J-P., 1999, Identification of shear wave parameters of viscoelastic solids by laboratory measurements of Stoneley-Scholte waves: Acustica, **85**, 505–516.

Glangeaud, F., Mari, J. L., Lacoume, J. L., Mars, J., and Nardin, M., 1999, Dispersive seismic surface waves on geophysics: European Journal of Environmental Engineering and Geophysics, **3**, 265–306.

Glorieux, C., Van de Roystyne, K., Gusev, V., Gao, W., Lauriks, W., and Thoen, J., 2002, Nonlinearity of acoustic waves at solid-liquid interfaces: Journal of the Acoustic Society of America, **111**, 95–103.

Granli, J. R., Arntsen, B., Sollid, A., and Hilde, E., 1999, Imaging through gas-filled sediments using marine shear-wave data: Geophysics, **64**, 668–677.

Gusev, V., Desmet, W., Lauriks, W., Glorieux, C., and Thoen, J., 1996, Theory of Scholte, leaky Rayleigh, and lateral waves via the laser-induced thermoelastic effect: Journal of the Acoustic Society of America, **100**, 1514–1528.

Hamilton, E. L., 1972, Compressional-wave attenuation in marine sediments: Geophysics, **37**, 620–646.

——— 1976, Attenuation of shear waves in marine sediments: Journal of the Acoustic Society of America, **60**, 334–338.

——— 1979, V_P/V_S and Poisson's ratios in marine sediments and rocks: Journal of the Acoustic Society of America, **66**, 1093–1101.

Hamilton, E. L., and Bachman, R. T., 1982, Sound velocity and related properties of marine sediments: Journal of the Acoustic Society of America, **72**, 1891–1904.

Holland, C. W., 1991, Surface waves in poro-viscoelastic marine sediments, *in* J. M. Hovem, M. D. Richardson, and R. D. Stoll, eds., Shear waves in marine sediments, Kluwer Academic Publishers, 13–20.

Kessler, D., and Kosloff, D, 1991, Elastic wave propagation using cylindrical coordinates: Geophysics, **56**, 2080–2089.

Kindelan, M., Seriani, G., and Sguazzero, P., 1989, Elastic modelling and its application to amplitude versus angle interpretation: Geophysical Prospecting, **37**, 3–30.

Komatitsch, D., Barnes, C., and Tromp. J., 2000, Wave propagation near a fluid-solid interface: A spectral element approach: Geophysics, **65**, 623–631.
Lomnitz, C., Butler, R., and Novarro, O., 2002, Coupled modes at interfaces: A review: Geofísica Internacional, **41**, 77–86.
Luke, B. A., and Stokoe, K. H., 1998, Application of SASW method underwater: Journal of Geotechnical Geoenvironmental Engineering, **124**, 523–531.
McMechan, G. A., and Yedlin, M. J., 1981, Analysis of dispersive waves by wave field transformation: Geophysics, **46**, 869–874.
Meegan, G. D., Hamilton, M. F., Ill'inski, Yu. A., and Zabolotskaya, E. A., 1999, Nonlinear Stoneley and Scholte waves: Journal of the Acoustic Society of America, **106**, 1712–1723.
Mittet, R., 2002, Free-surface boundary conditions for elastic staggered-grid modeling schemes: Geophysics, **67**, 1616–1623.
Muyzert, E., 2000, Scholte wave velocity inversion for a near surface S-velocity model and PS-statics: 69th Annual Internation Meeting, Society of Exploration Geophysics, Expanded Abstracts, 1197–1200.
Nolet, G., and Dorman, L. M., 1996, Waveform analysis of Scholte modes in ocean sediment layers: Geophysical Journal International, **125**, 385–396.
Padilla, F., de Billy, M., and Quentin, G., 1999, Theoretical and experimental studies of surface waves on solid-fluid interfaces when the value of the fluid sound velocity is located between the shear and the longitudinal ones in the solid: Journal of the Acoustic Society of America, **106**, 666–673.
Paillet, F. L., and White, J. E., 1982, Acoustic modes of propagation in the borehole and their relationship to rock properties: Geophysics, **47**, 1215–1228.
Phinney, R. A., 1961, Propagation of leaking interface waves: Bulletien of the Seismic Society of America, **51**, 527–555.
Prasad, M., 1998, Empirical trends in velocity and quality factor properties of reservoir rocks: 68th Annual Internation Meeting, Socoety of Exploration Geophysics, Expanded Abstracts.
Rauch, D., 1980, Experimental and theoretical studies of seismic interface waves in coastal waters, *in* W. A. Kupermann and F. B. Jensen, eds., Bottom-interacting ocean acoustics: Plenum Press, 307–327.
Robertsson, J. O. A., and Levander, A., 1995, A numerical study of seafloor scattering: Journal of the Acoustic Society of America, **97**, 3532–3546.
Roever, W. L., T. F. Vining, and E. Strick, E., 1959, Propagation of elastic wave motion from an impulsive source along a fluid/solid interface: Philosophical Transactions of the Royal Society of London, A, **251**, 456–465.
Scholte, J. G., 1942, On the Stoneley wave equation: Proceedings of the Koninklijke Nederlandse Akademie van Weten Schappen, **45**, 20–25, 159–164.
Schmidt, H., and Jensen, F. B., 1985, A full wave solution for propagation in multilayered viscoelastic media with application to Gaussian beam reflection at fluid-solid interfaces: Journal of the Acoustic Society of America, **77**, 813–825.
Stephen, R. A., 1986, Finite difference methods for bottom interaction problems, *in* D. Lee, Sternberg, R. L., and Schultz, M. H. eds., Computational acoustics, wave propagation: North-Holland, 225–238.
Stephen, R. A., and Bolmer, S. T., 1985, The direct wave root in marine seismology: Bulletin of the Seismic Society of America, **75**, 57–67.
Stephen, R. A., and Swift, S. A., 1994, Finite difference modeling of geoacoustic interaction at anelastic seafloors: Journal of the Acoustic Society of America, **95**, 60–70.
Strick, E., 1959, Propagation of elastic wave motion from an impulsive source along a fluid/solid interface. Part II: Theoretical pressure response. Part III: The pseudo-Rayleigh wave: Philosophical Transactions of the Royal Society of London, A, **251**, 465–523.
Stoll, R., Bryan, G., and Bautista, F., 1994, Measuring lateral variability of sediment geoacoustic properties: Journal of the Acoustic Society of America, **96**, 427–438.
Takeuchi, H., and Saito, M., 1972, Seismic surface waves, *in* B. A. Bolt, ed., Seismology: Surface waves and earth oscillations: Academic Press, 217–295.
Tessmer, E., Kessler, D., Kosloff, D., and Behle, A., 1992, Multi-domain Chebyshev-Fourier method for the solution of the equations of motion of dynamic elasticity: Journal of Computational Physics, **100**, 355–363.
van Vossen, R., Robertsson, J. O. A., and Chapman, C. H., 2002, Finite-difference modeling of wave propagation in a fluid-solid configuration: Geophysics, **67**, 618–624.
Winkler, K., and Nur, A., 1979, Pore fluids and seismic attenuation in rocks: Geophysical Research Letters, **6**, 1–4.
Zener, C., 1948, Elasticity and anelasticity of metals: University of Chicago Press.